Flame Spray Pyrolysis Synthesis and Aerosol Deposition of Nanoparticle Films

Antonio Tricoli
Dept. of Mechanical and Process Engineering, Particle Technology Laboratory, ETH Zurich, CH-8092, Zurich, Switzerland

Tobias D. Elmøe
Dept. of Chemical and Biochemical Engineering, Technical University of Denmark, DK-2800 Lyngby, Denmark

DOI 10.1002/aic.13739
Published online February 17, 2012 in Wiley Online Library (wileyonlinelibrary.com).

The assembly of nanoparticle films by flame spray pyrolysis (FSP) synthesis and deposition on temperature-controlled substrates (323–723 K) was investigated for several application-relevant conditions. An exemplary SnO_2 nanoparticle aerosol was generated by FSP and its properties (e.g., particle size distribution), and deposition dynamics were studied in details aiming to a simple correlation between process settings and film growth rate. At high precursor concentrations (0.05–0.5·mol/L), typically used for FSP synthesis, the nanoparticles agglomerated rapidly in the aerosol leading to large (>100 nm) fractal-like structures with low diffusivity. As a result, thermophoresis was confirmed as the dominant nanoparticle deposition mechanism down to small (≈40 K) temperature differences (ΔT) between the aerosol and the substrate surface. For moderate-high ΔT (>120 K), thermal equilibrium was rapidly obtained yielding a constant thermophoretic flux and film growth rate. A model was developed to predict the nanoparticle deposition rates by FSP synthesis at moderate-high ΔT that does not require detailed analysis of the aerosol composition. Comparison with previous studies having similar nozzle geometries showed that the deposition rates of FSP-made aerosols can be reasonably well predicted for various materials and flame conditions. © 2012 American Institute of Chemical Engineers *AIChE J,* 58: 3578–3588, 2012
Keywords: aerosols, combustion, deposition methods, mass transfer, films

Introduction

Nanoparticles have, since long, become an important component of several technologies such as catalysts,[1] sensors,[2] solar cells,[3] and batteries.[4] In addition to nanoparticle synthesis, a critical step is their deposition onto the target substrates that commonly results in the formation of a porous film.[5–7] Deposition is often achieved by wet-phase processing of nanoparticle solutions such as screen printing, drop-, dip-, and spin-coating. These methods are easily applicable on most substrates and result in mechanically stable film morphologies. However, they offer only limited control over the resulting film properties (e.g., porosity, morphology), require several steps and long process time for evaporation of binders and solvents. A promising alternative for nanoparticle film synthesis is their direct self-assembly from the gas phase by deposition of nanoparticle-laden aerosols.

Recently, aerosol deposition of nanoparticles has been successfully applied to the fabrication of antifogging coatings,[8] gas sensors,[6,7,9–11] fuel cells,[12] solar cells,[13] phosphor screens,[14] LiMn-based batteries,[15] and catalyst-coated substrates.[16] At moderate substrate temperatures, the morphology of aerosol-deposited films is mainly determined by the ratio between Brownian diffusion and deposition velocity (Péclet number, Pe)[17–20] allowing superior reproducibility of structure-related functionalities.[6] Selection of aerosol size fraction allows deposition of nearly monodisperse nanoparticles possibly improving performances as shown by differential mobility analyzer (DMA)[9] and Berner low-pressure impactor (BLPI).[21] Furthermore, accurate control of the aerosol concentration and/or charging resulted in unprecedented miniaturization of nanoparticle films both in terms of thickness (1–100 nm)[11] and horizontal spreading (10–500 nm).[5] However, translating these results into industrial products requires scalable nanoparticle sources and tight control over the resulting aerosol properties (e.g., particle coalescence,[20,22] air entrainment[23]), as well as sufficient understanding of the main mechanisms controlling the film growth dynamics (e.g. aerosol and substrate surface temperatures)[24] at the used deposition conditions.

Among aerosol synthesis technologies, flame processes have demonstrated very high production rates and are, since long, used for industrial production of several nanoparticle commodities.[25] In particular, liquid-fed spray flames[26,27] are a versatile option offering a large spectrum of precursors and able to synthesize metal, salt, and oxides nanoparticles.[28] Recently, spray flame synthesis has enjoyed increasing interest from the scientific community resulting in the development of several systems, often based on external-mix, two-fluid nozzles, such as flame spray pyrolysis (FSP)[29] and

Correspondence concerning this article should be addressed to A. Tricoli at tricoli@ptl.mavt.ethz.ch.
Current Address of Tobias D. Elmøe: Amminex A/S, DK-2860 Soeborg, Denmark.

Table 1. FSP Settings Used in This Work

Precursor	Tin (II)-ethylhexanoate	Titanium (IV)-isopropoxide
Solvent	Xylene	Xylene
Precursor concentration (C_{pr}), mol/L	0.1, 0.5	0.5
Precursor feed rate ($\dot{V}_{pr}$), mL/min	5	5
Dispersion O_2 flow rate ($\dot{V}_{gas}$), L/min	5	5
Nozzle pressure drop, bar	1.5	1.5
Premixed CH_4 flow rate, L/min	1.5	1.5
Premixed O_2 flow rate, L/min	3.2	3.2
Sheath O_2 flow rate, L/min	5	5
Deposition height (HAB), cm	20	20
Substrate holder temperature (T_B), K	323–723	323

All the gas flow rates are reported at standard temperature and pressure (STP).

liquid flame spray.[27] However, accurate prediction and control of the properties of liquid-fed spray flame aerosols remains challenging. In fact, such two-phase systems have different air entrainment properties than single-phase (e.g., vapor-fed) flames[23] leading to strongly nozzle-dependent concentration and temperature profiles. In addition, the high primary particle concentration, usually obtained during liquid-fed spray flame synthesis, leads to the rapid formation of large agglomerates[8,21] with reduced diffusivity and drastically different film properties than that expected for nonagglomerated particles.[20,22] In this respect, a model for the prediction of the growth rate of nanoparticle films made by spray flames at high precursor concentration would greatly facilitate the engineering of their properties and industrial utilization.

The deposition rate of nanoparticles from hot aerosols to cold substrates at high Schmidt (Sc) and low Stokes (St) numbers is typically controlled by thermophoresis.[24,30] For very fine nanoparticles and small temperature gradients, Brownian diffusion may become comparable to thermophoresis leading, for example, to the leakage of small particles in the dust-free layer of a hot wall.[30] The effect of the particle-size distribution cannot be neglected *a priori* as the thermophoretic coefficient may vary with the Knudsen (*Kn*) number[22] especially for particles having high thermal conductivity. Deposition of fractal-like particles, for example, can result in different thermophoretic flux than those expected for completely dense spheres having the same mobility diameter.[22,31] Furthermore, films made of such fractal-like particles have very high porosity (e.g., >96%) even for the limit of ballistic deposition (Pe > 100) and, thus, their visible thickness is considerably higher than that expected from gravimetric measurements. As a result, a widespread model for the deposition of nanoparticles and film growth by liquid-fed spray flames is still missing.

Here, the aerosol deposition of nanoparticles synthesized by unconfined FSP on temperature-controlled substrates was investigated at high precursor solution concentrations (0.1–0.5 mol/L). An external-mix, two-fluid nozzle was used to spray combustible solutions of organometallic precursor. This spray was ignited by a surrounding premixed CH_4/O_2 flame leading to the formation of a hot aerosol of metal oxide nanoparticles. The properties of an exemplary FSP-made SnO_2 aerosol were investigated and used to model the deposition dynamics of such concentrated aerosols. More in details, the morphology of these FSP-made SnO_2 particles was investigated by transmission electron microscopy (TEM) analysis upon their collection from the gas phase by thermophoretic sampling (TS) and filtration. The main SnO_2 aerosol properties such as air entrainment, particle concentration, and mobility size distribution were investigated as a function of the height above the burner (HAB). The particle deposition dynamics was studied with respect to the measured aerosol and substrate properties leading to a correlation between deposition rates and flame conditions. Finally, this model was validated by comparison with the deposition rates measured here for TiO_2 aerosols and with that previously reported for similar external-mix, two-fluid nozzles.

Experimental

Aerosol synthesis and characterization

The SnO_2 and TiO_2 nanoparticle-laden aerosols were prepared as follows (Table 1): tin (II)-ethylhexanoate (Aldrich, purity >98%) or titanium (IV)-isopropoxide. (Aldrich purity >97%) were diluted in xylene (Fluka, purity >98.5%) to the target (0.1–0.5 mol/L) metal atoms concentration. This solution was supplied (Figure 1) at a rate of 5 mL/min through an external mix, two-fluid nozzle, described elsewhere in details,[29] and dispersed into a fine spray with 5 L/min oxygen (pressure drop 1.5×10^5 Pa). The spray was ignited by a supporting ring-shaped premixed methane/oxygen flame (CH_4 = 1.5 L/min, O_2 = 3.2 L/min). Additional 5 L/min sheath oxygen was supplied from an annulus surrounding that flame to ensure excess oxidant flow. Powder samples were collected with a vacuum pump (Vacuumbrand, RE 16) on a water-cooled glass-fiber filter (GF/D Whatman, 0.257 m diameter) placed at 50 cm HAB. The SnO_2 aerosol concentration

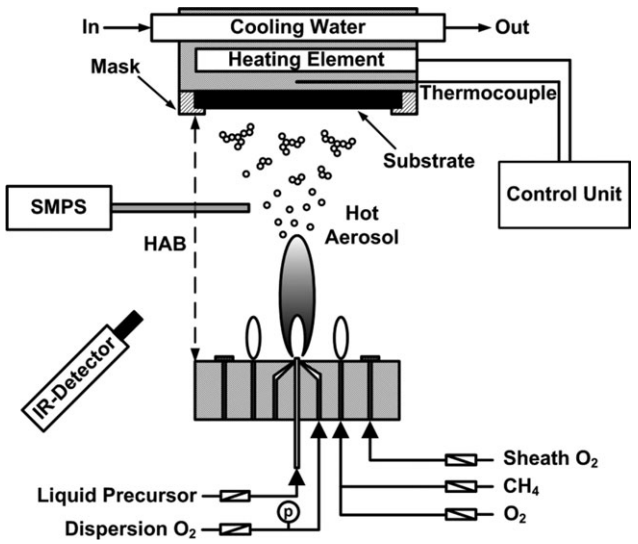

Figure 1. Schematic of the FSP burner and temperature-controlled substrate holder used for nanoparticle synthesis and deposition.

A two-phase, external-mix nozzle was used to spray a combustible liquid precursor solution. The spray was ignited by a supporting premixed CH_4/O_2 flame leading to the formation of a nanoparticle aerosol. The nanoparticles were deposited on a temperature-controlled substrate by orthogonal impingement of the aerosol.

was measured by a scanning mobility particle sizer (SMPS) consisting of a DMA (TSI model 3071) and a condensation particle counter (TSI model 3022A). The SMPS measured the mobility number size distribution in the range of 11–514 nm of the cooled and diluted (1:10 by volume) aerosol. The aerosol for the SMPS analysis was collected in the proximity of the substrate holder for direct deposition of nanoparticles (Figure 1), while varying the HAB between 20 and 40 cm. TS[32] of the aerosol was performed for 40 ms on TEM grids (carbon type B copper 200 mesh, Ted Pella) at 13 cm HAB to ensure complete evaporation of the sprayed precursor solution.

Nanoparticle deposition

The nanoparticles were deposited by orthogonal impingement of the FSP-made aerosols onto a temperature-controlled substrate holder (Figure 1) placed at 20 cm HAB. The substrates were either 0.1-mm thick steel or 1-mm thick alumina plates with an aerosol-exposed area of 2.1×1.6 cm^2. The substrate holder temperature (T_B) was measured 0.5 cm below its surface by an *n*-type thermocouple, whereas substrate surface temperature (T_S) was measured by an infrared camera (Fluke, Ti55FT) calibrated (emissivity for $Al_2O_3 = 0.75$) by fixing the substrate temperature with the integrated substrate holder heater. The aerosol temperature (T_F) in the proximity of the substrate was 773 K as measured by an *n*-type thermocouple placed slightly upstream of the substrate, and it was in agreement with the reported values[6] for a similar FSP deposition setup. For each deposition experiment, a substrate holder temperature between 323 and 773 K was set to control the surface temperature and, thus, investigate the effect of the driving temperature difference ($\Delta T = T_F - T_S$) on the nanoparticle deposition rate. The deposited nanoparticles mass was determined by gravimetric analysis (Mettler Toledo, XS204) of the substrate before (e.g., 614.57 mg) and after deposition (e.g., 615.8 mg). The film thickness and morphology were investigated by scanning electron microscopy (SEM) with a LEO 1530 Gemini (Zeiss/LEO, Oberkochen).

Results and Discussion

Nanoparticle synthesis and aerosol characterization

Figure 1 shows a schematic of nanoparticle film assembly by aerosol deposition. First, a nanoparticle (SnO_2 or TiO_2) aerosol was generated (Figure 1) by combustion of an organometallic precursor solution sprayed by an external mix, two fluid nozzle. Thereafter, orthogonal impingement of this hot aerosol on a temperature-controlled substrate led to nanoparticle deposition and film growth. Here, the flame settings (e.g., precursor concentration, feed rate, and dispersion gas flow) were chosen (Table 1) accordingly to those commonly reported[6,7,33,34] for FSP-synthesis of a broad range of metal oxide nanoparticles. These conditions ensure sufficient dispersion of the precursor solution and oxygen concentration leading to the formation of metal oxide nanoparticles with high purity as reported for SnO_2[33] and several other materials.[29,35] More in details, a total of 0.59 mol/min O_2 were supplied by dispersion, sheath, and premixed flame flows (Figure 1), whereas full combustion of the liquid precursor solution and CH_4 required 0.61 mol/min resulting in slightly under-stoichiometric conditions. However, the high surrounding air entrainment of such spray flames[23] resulted in fuel lean combustion and no soot formation.[36] This allowed an accurate characterization of the aerosol properties in terms of primary particle and mobility sizes by means of TS and SMPS.

Figure 2 shows TEM images of SnO_2 particles (Table 1, $C_{pr} = 0.5$ mol/L) collected by TS slightly downstream of the flame tip (13 cm HAB). The particles had a fractal-like morphology (Figure 2a) and a broad size distribution reaching several hundred nm in diameter. Their structure was fairly open (Figure 2b,c) in comparison to SnO_2 particles made by vapor-fed flames.[37] This is attributed to the high air entrainment in FSP systems[23] that results in rapid cooling of the aerosol and, thus, limited coalescence of the agglomerate structure. At higher magnification (Figure 2d), the primary particle diameter (d_p) was about 10 nm. The broad sintering necks (Figure 2d) indicated the formation of hard agglomerates in line with the high temperatures (>2200 K) previously measured[29] for similar FSP settings. The primary particle diameter did not increase further with increasing HAB as determined by TEM (Figure 2d, inset) analysis of SnO_2 powders filter-collected at 50 cm HAB. This indicates that, at 13 cm HAB, the primary particle growth had become significantly slow and further increase of the mobility and/or aerodynamic diameters were mainly due to agglomeration. These results are in good agreement with the x-ray diffraction (XRD) ($d_{XRD} \approx 10$ nm),[7] count mode ($d_{po} = 9.5$ nm), and geometric mean ($d_{pe} = 10.4$ nm) diameters reported[21] for FSP-made SnO_2 powders for the same process conditions.

The agglomeration process was monitored online by SMPS analysis (Figure 3) of the SnO_2 aerosol as a function of the HAB. Up to 15 cm HAB, the SnO_2 particle number concentration was above the detection limit of the SMPS at the used dilution factor (1:10) and, thus, the size distribution is not reported. At 20 cm HAB (Figure 3), the mobility mode and geometric mean diameter were 131 and 137 nm, respectively, with a geometric standard deviation (GSD) of 1.6. This GSD value is above the self-preserving one (1.47) for spherical particles in the free molecular regime[38] but in agreement with the self-preserving size distribution of agglomerates[39] with fractal dimension (D_f) of 2–2.3 at moderate concentrations.[40] Deviations from the self-preserving GSD for Brownian coagulation are also attributable to the contribution of turbulence-induced coagulation.[41] Increasing the sampling HAB to 20 and 30 cm (Figure 3) decreased the particle concentration in line with the increased surrounding air entrainment. Furthermore, it decreased the mode and geometric mean diameter to 126 and 109 nm, respectively, while slightly increasing the GSD from 1.61 to 1.63. This further broadening of the GSD, as well as the variation in geometric mean diameter, are attributed to the re-entrainment of side streamlines having different particle concentration, temperature, and residence time profiles, than those at the center line. The count mobility mode (131–109 nm) and geometric mean (137–111 nm) diameters, measured here, are comparable to the mass aerodynamic mode (118 nm) and geometric mean (162 nm) diameters previously measured by BLPI[21] for the same FSP-made SnO_2 aerosol.

Air entrainment and aerosol concentration

Independently of the deposition mechanism (e.g., thermophoresis, Brownian diffusion, and impaction), correct estimation of the particle concentration is necessary for computation of their deposition (and film growth) rate, as, in unconfined jets, the initial precursor concentration is considerably diluted

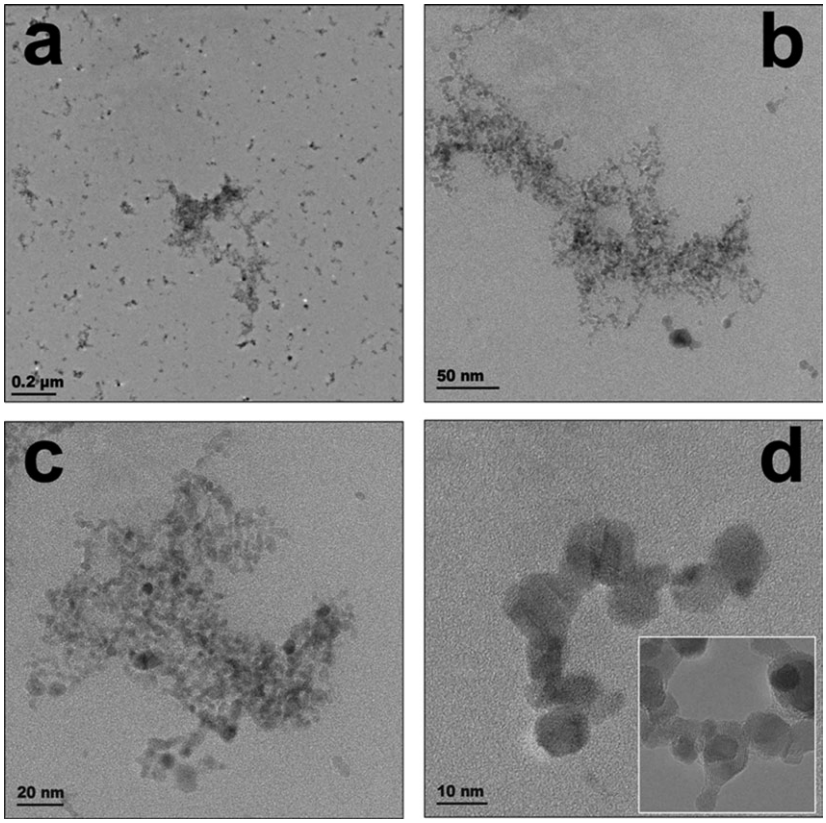

Figure 2. TEM images of SnO_2 nanoparticles collected by TS at 13 cm HAB.

Large agglomerates (a,b) constituted of small primary particles (d_{TEM} = 10 nm) were collected (c,d). The SnO_2 primary particle size at 13 cm HAB (a–d) was comparable to that of the same SnO_2 powder collected at 50 cm HAB (d, inset) by a filter.

by the entrainment of surrounding air. This task is quite challenging for spray flames as a two-phase dynamics should be considered that may diverge considerably from that expected for single-phase nozzle.[23]

In this study, the air entrainment up to 20 cm HAB was computed from the measured aerosol temperature, the supplied enthalpy, and gas flow rates. More in details, full combustion of the supplied (Table 1, SnO_2) precursor solution and CH_4 flow rates (Figure 1) summed up to a total enthalpy feed rate of 234 kJ/min. Neglecting radiative cooling of the aerosol, a total gas flow of 359.8 L/min (at STP) was necessary to reach the measured aerosol temperature (T_F = 773 K) at 20 cm HAB. Considering only the gas and fluid flow rates (Table 1) supplied through the nozzle (Figure 1), this resulted in a total entrainment of 353.2 L/min at STP and in a dilution factor (F_d) of 54 in the first 20 cm HAB.

In unconfined gas jets, the total mass flow rate ($\dot{m}_t$) increases linearly with the height above the nozzle/burner (HAB)[42]

$$\frac{\dot{m}_t}{\dot{m}_i} = K_e \frac{HAB}{d} \quad (1)$$

where $\dot{m}_i$ is the initial mass flow rate supplied to the nozzle, d is the gas nozzle diameter, and K_e is the entrainment constant, generally increasing from 0.1 to 0.32 in the first 10 d above the nozzle.[42] Here, however, the gas nozzle diameter (d_g) was not sufficient to describe the air entrainment dynamics as about 39% of $\dot{m}_i$was fed by the liquid precursor through a nozzle having an internal diameter (d_L) of 0.6 mm and the residual 61% was fed directly (Figure 1) in the gas phase by the dispersion oxygen through an annular opening. An annular opening area of 0.25 mm^2 was computed, as previously suggested,[29] for the used flame settings (Table 1) resulting in an equivalent gas nozzle (d_g) diameter[23] of 0.57 mm. A total nozzle diameter (d) of 1.17 mm was computed summing the liquid (d_L) and equivalent gas nozzle diameters (d_g). According to Eq. 1, this resulted in an entrainment constant (K_e) of 0.23 in

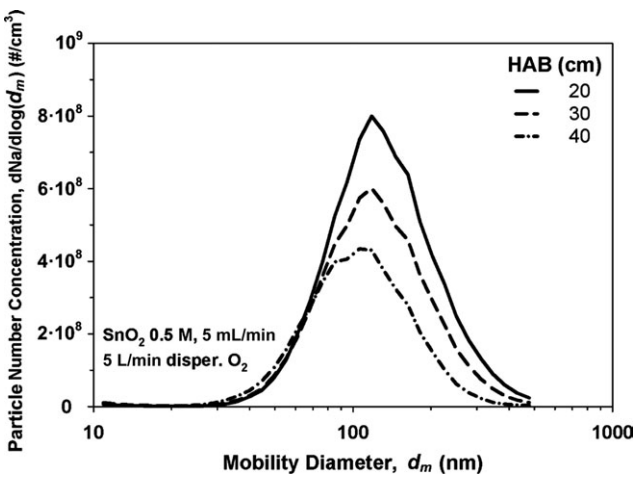

Figure 3. Mobility diameter (d_m) number size distribution of the FSP-made SnO_2 aerosol measured by the SMPS at several HAB.

The SMPS measurements are in good agreement with the TEM analysis showing a large number of particles (agglomerates) with size above that of the primary particles (10 nm).

Table 2. Summary of Flame Conditions and Film Growth Rates Reported for Vapor- and Liquid-Fed Flame Deposition of Nanoparticles at the Deposition Height

		Precursor		Primary Particles		Temperature		Film					
Flame Type	Material	Concentration (mol/L)	Feed-Rate (L/min)	Diameter (nm)	Concentration (#/m^3)	Gas (K)	Substrate (K)	Deposition Height (cm)	Thickness (μm)	Porosity (%)	Bulk Growth Rate (μm/min)	Molar Growth Rate (mol/min cm^2) $\times 10^{-6}$	Reference
Vapor-fed	SnO_2, SiO_2	–	–	–	–	≈1500	≈348–800	2–3	0.5–10	–	(1)[a]	(4.4)[a]	43
Vapor-fed	TiO_2	1.1–9.2 $\times 10^{-6}$ (mol/min)		4.5–8	≈10^{21}	≈2200	≈750–1080	2	0.04–2	–	(0.026–0.67)[a]	(0.12–3.2)[a]	53
Liquid-fed	SnO_2	–	–	<30 nm	–	–	1123	–	1	–	(0.05)[a]	(0.23)[a]	44
Liquid-fed	Au:TiO_2	0.7	–	4	–	–	≈323	5–15	50–150	90–79	0.25–1.5	1.2–7.2	16
Liquid-fed	$Ce_{0.8}Gd_{0.2}O_2$	0.00006	5 $\times 10^{-4}$	–	–	–	473	12	0.56	Dense	0.028	–	45
Liquid-fed	$Ba_xSr_{1-x}TiO_3$	–	–	–	–	1323	≈1273	7.9–10.8	0.4	Dense	0.009–0.006	–	46
Liquid-fed	Eu:Y_2O_3	0.5	1.2 $\times 10^{-2}$	24	–	–	–	25	239	97	0.41	0.91	14
Liquid-fed	TiO_2	0.05	5 $\times 10^{-3}$	≈ 5	–	773	–	20	0.34	≈98	0.02	0.096	8
Liquid-fed	SnO_2	0.5	5 $\times 10^{-3}$	10.5	–	773	393	20	≈40	98	0.133	0.61	6
Liquid-fed	SnO_2	0.5	5 $\times 10^{-3}$	10	≈2.94 $\times 10^{17}$	773	323–723	20	≈70	98	0.073–0.22	0.34–1	This work

[a]The visible film growth rate was reported and used for computation of the molar growth rate as the bulk growth rate was not available.

the first 20 cm HAB. The K_e, computed here, is reasonably close to that (0.21) computable with the same procedure from the air entrainment[23] measured in larger FSP burners.

The SnO_2 aerosol concentration was estimated from its production rate and the air entrainment determined above. For a SnO_2 precursor solution concentration (C_{pr}) of 0.5 mol/L (Table 1), a primary particle production rate of 1.1 $\times$ 10^{17} #/min was computed assuming a spherical primary particle shape with a diameter of 10 nm in line with the TEM (Figure 2d) and XRD analysis of the collected SnO_2 powder. Considering the total gas flow computed above, this results in a SnO_2 primary particle concentration (N_p) of 2.94 $\times$ 10^{17} #/m^3 at 20 cm HAB and STP. With respect to aerosol deposition of nanoparticle films (Table 2), this primary particle production rate and concentration are remarkably high and justify the large agglomerates, observed here, lightly downstream of the flame tip (Figure 2). In fact, even for 10 times lower precursor concentrations (C_{pr}), FSP-made TiO_2 nanoparticles (Table 2) were found to form large (>50 nm) agglomerates at about 15 cm HAB.[8] Other aerosol synthesis methods such as evaporation–condensation processes lead to considerably lower (10^{11}–10^{14} #/m^3) primary particle concentrations decreasing the film growth rates but allowing deposition of nonagglomerated particles.[47,48]

The primary particle concentration (N_p) of the SnO_2 aerosol (C_{pr} = 0.5 mol/L) was also estimated from the mobility diameter number size distribution measured by SMPS (Figure 3) accounting for the formation of agglomerates.[49–51] Rogak et al.[49] suggested that the number of primary particles in an agglomerate (N_{p_dm}) and its mobility diameter d_m (Figure 4a, continuous line) are correlated by the following equation

$$d_m = \beta d_p \sqrt{\frac{D_f}{D_f + 2}} N_{p\_dm}^{1/D_f} \quad (2)$$

where D_f is the fractal dimension and β is a constant between 0.7 and 1, [49] here set as 0.9.

With the primary particle diameter (d_p) of 10 nm, estimated above, and integrating N_{p_dm} (Figure 4a) in Eq. 2 over the mobility diameter number size distribution measured here at 20 cm HAB (Figure 3, continuous line), the total primary particle concentration (N_p) becomes a function of the assumed D_f and increases from 1.4 $\times$ 10^{17} to 7.1 $\times$ 10^{17} #/m^3 (at STP) with D_f increasing from 1.8 to 2.3. A N_p of 2.65 $\times$ 10^{17} #/m^3 was computed at 20 cm HAB assuming a D_f of 2 in line with the D_f (1.9–2) measured[52] for FSP-made SiO_2 nanoparticles. This N_p is reasonably close to that (2.94 $\times$ 10^{17} #/m^3) estimated above from the air entrainment and precursor feed rate.

Lall et al.[50] suggested that the number of primary particle per agglomerate (N_{p_dm}) can be estimated (Figure 4a, pointed line), up to a D_f of 2, without prior knowledge of the agglomerate density by the following correlation between d_m and N_{p_dm}

$$d_m = \frac{C^* N_{p\_dm} C(d_m) d_p^2}{3\pi\lambda} \quad (3)$$

where C^* is a constant set to 9.17, in line with that reported[50] for agglomerates with random orientation, $C(d_m)$ is the Cunningham correction factor for an agglomerate of size d_m and λ is the mean free path of the medium. Integration of Eq. 3 over d_m resulted (Figure 4b, triangles) in an N_p of 7.3 $\times$ 10^{16} #/m^3 and, thus, four times lower than that estimated above

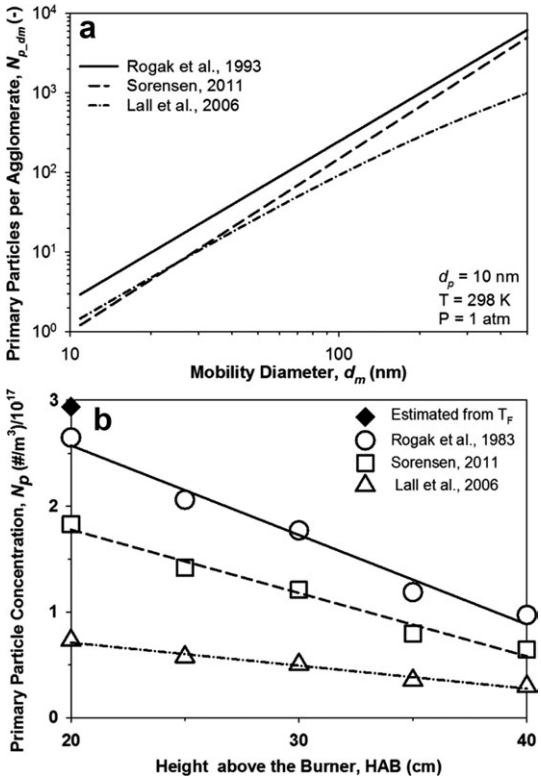

Figure 4. Number of primary particle (a) in an agglomerate as function of its mobility diameter computed according to Rogak et al. (1993) (continuous line),[49] Sorensen (2011) (broken line),[51] and Lall et al. (2006) (dotted line).[50]

Primary particle concentration (b) as a function of the HAB computed for the above correlations (empty symbols) and estimated from the aerosol temperature (diamond).

from air entrainment at 20 cm HAB. Achievement of such low particle concentrations (7.3×10^{16} #/m^3) at 20 cm HAB would require an air entrainment of about 1430 L/min at STP resulting in a very high dilution factor. As a result, Eq. 3 appears to underestimate the actual N_p at 20 cm HAB. Sorensen (2011)[51] also proposed a D_f-free computation of N_{p_dm} for an agglomerate of size d_m in the free molecular

$$d_m = d_p N_{p\_dm}^{0.46} \tag{4}$$

and in the continuum regime

$$d_m = d_p N_{p\_dm}^{0.46}, \quad N_{p\_dm} < 100 \tag{5a}$$

$$d_m = 0.65 d_p N_{p\_dm}^{0.56}, \quad N_{p\_dm} > 100 \tag{5b}$$

Equations 4 and 5 result (Figure 4b, squares) in a $N_p = 1.8 \times 10^{17}$ #/m^3 at 20 cm HAB and STP that is reasonably close to that (2.65×10^{17} #/m^3) computed by Eq. 2 with a $D_f = 2$ and to that (2.94×10^{17} #/m^3) estimated from the precursor feed rate and air entrainment.

Figure 4b shows the total primary particle concentration (N_p) as a function of the HAB computed from Eqs. 2 to 5, and the measured mobility diameter number size distributions (Figure 3). For comparison, the primary particle concentration, estimated above from the air entrainment at 20 cm HAB, is also reported (Figure 4b, diamond). For all computations (Figure 4b), N_p decreased always linearly with increasing HAB ($R^2 > 0.97$). This is in agreement with the expected linear entrainment of surrounding air with increasing distance from the nozzle/burner in unconfined jets.[42] The good agreement with the computation of N_p along Eq. 2 and $D_f = 2$ (Figure 4b, circles) and its estimation (Figure 4b, diamond) indicates that a N_P of about 2.94×10^{17} #/m^3 and a K_e of 0.23 are reasonable guesses of the SnO_2 aerosol ($C_{pr} = 0.5$ mol/L) primary particle concentration and entrainment constant at 20 cm HAB, and, thus, were used further for computation of the nanoparticle deposition rates.

Particle deposition and film growth

For SnO_2 nanoparticle deposition ($C_{pr} = 0.5$ mol/L) at 20 cm HAB (Figure 1), the resulting film morphology was studied by SEM and gravimetric analysis. These films had a homogeneous thickness (Figure 5a) over several hundred μm indicating a uniform nanoparticle flux toward the substrate surface. The film surface morphology (Figure 5b,c) was characterized by a fragile structure constituted by thin bridges enclosing large pores (diameter >1 μm). At larger magnification (Figure 5d), the bridges were reveled to be constituted by tiny nanostructures with size comparable to the primary particles (10 nm) collected by TS at 13 cm HAB (Figure 2). In fact, at the 20 cm HAB, the aerosol temperature ($T_F = 773$ K) was too low to induce measurable sintering of the SnO_2 nanoparticles within the deposition time ($t_d = 1$–6 min)[6,7] suggesting that the film morphology (Figure 5) was mainly determined by the nanoparticle deposition dynamics. In contrast, at higher substrate temperatures and lower HAB, the morphology of flame-made TiO_2 films[53] was reported to change considerably due to coalescence during deposition.

In the absence of electrostatic forces, the main nanoparticle deposition mechanisms are Brownian diffusion, thermophoresis, and impaction. Inertial deposition (or impaction) is characterized by the Stokes number

$$\mathrm{St} = \frac{\tau \cdot U_0}{\delta} \tag{6}$$

where τ is the relaxation time ($\approx 10^{-8}$ s, for nanoparticles),[54] U_0 is the particle velocity and δ is the boundary layer thickness in the range of 0.01–1 mm[55] in the stagnation point for typical FSP Reynolds number ($Re \approx 5 \times 10^4$).[6] Impaction can be neglected for St smaller than the critical one for orthogonally impinging jets ($\mathrm{St_{crit}} = 0.24$).[54] For similar flame-spray pyrolysis reactors, it was reported[23] that the maximal gas jet velocity decreases below 100 m/s in the first 3 cm HAB. Here, the deposition height was set to 20 cm HAB and, thus, considerably smaller ($U_0 \ll 100$ m/s) gas velocities are expected resulting in St $\ll 0.1$ even for very small boundary layer thickness (e.g., 0.01 mm). As a result, deposition by impaction was neglected.

The mass transfer to the substrate is described for each particle/agglomerate with mobility size of d_m by the following differential equation for their number concentration ($N_a(d_m)$)[30]

$$\frac{\partial N_a(d_m)}{\partial t} + \underline{\nabla} \cdot (v + v_T) N_a(d_m) = \underline{\nabla} \cdot (D_{dm} \underline{\nabla} N_a(d_m)) \tag{7}$$

where v is the fluid velocity, v_T is the thermophoretic velocity, and D_{dm} is the corresponding diffusion coefficient. The thermophoretic velocity (v_T) is usually described as

$$v_T = -k_T \frac{\mu_F}{\rho_F} \nabla \ln T \tag{8}$$

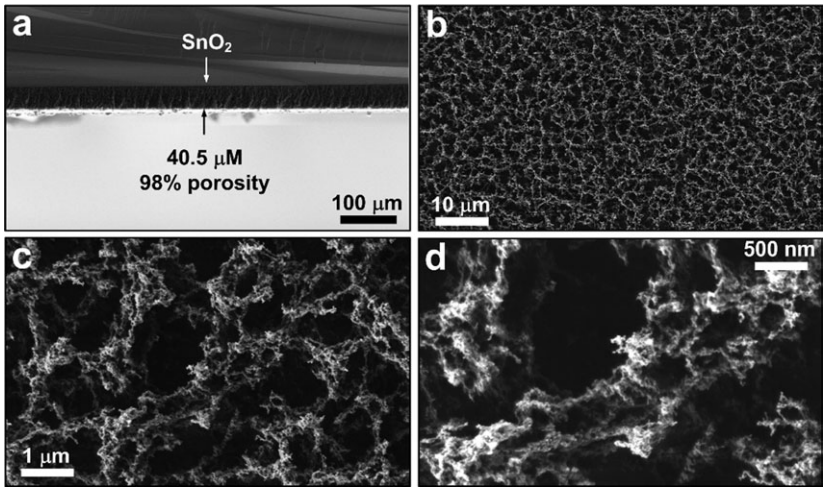

Figure 5. SEM cross-sectional (a) and top (b–d) views of a SnO_2 nanoparticle film aerosol deposited (C_{pr} = 0.5 mol/L) deposited for 4 min.

A uniform film thickness (a) is observed all over the substrate surface. The (b–d) films are highly porous and the primary particle size (d) observed by TS analysis is still preserved.

where μ_F and ρ_f are the fluid dynamic viscosity and density, respectively, and k_T is the thermophoretic coefficient. In the free molecular regime ($Kn \gg 1$), k_T is usually considered independent of the particle size and set equal to 0.55.[56] For the continuum ($Kn \ll 1$) and transition regime ($Kn \approx 1$), however, k_T is described by[56]

$$k_T = 2C(d_m)c_s \frac{k^* + c_t Kn}{(1 + 3c_m Kn)(1 + 2k^* + 2c_t Kn)} \quad (9)$$

where k^* is the ratio of the thermal conductivity of the fluid and particles, c_m, c_s, and c_t are the momentum exchange, thermal slip, and temperature jump coefficients set to 1.146, 1.147, and 2.18,[57] respectively. For computation of k^*, the poor heat conduction through fractal-like particles should be taken into account leading to[22] $k^* \approx 1$ as it was further confirmed[31] for thermophoretic deposition of soot agglomerates. Figure 6a shows the thermophoretic coefficient (k_T), computed here, as a function of Kn with T_F = 773 K and T_B = 323 K for the measured particle mobility size distribution (10–500 nm) with $k^* = 1$ (solid line)[22] and $k^* = 4.7 \times 10^{-4}$ (broken line) as resulting from the ratio between thermal conductivity of air and SnO_2.[56] For $k^* = 4.7 \times 10^{-4}$ (Figure 6a, broken line), k_T diverged considerably from 0.55 with decreasing Kn. In contrast, accounting for the poor thermal conduction in agglomerates ($k^* = 1$) led to a fairly constant k_T through the whole transition regime. These results are in good agreement with that reported for thermophoretic deposition of soot agglomerates (d_m = 34–300 nm) in the transition regime.[31] Furthermore, higher substrate holder temperatures ($T_B > 323$ K) would lead to higher particle temperatures (T_p) and, thus, even higher Kn resulting in k_T closer to 0.55. Hence, here, a $k_T = 0.55$ was used independently of the particle size as it was always (d_m = 10–500 nm) within 2.1% accuracy (Figure 6a, continuous line) from that computed with Eq. 9 and $k^* = 1$ for all T_B considered.

As a result, the total primary particle flux (j_{tot}) to the substrate can be computed in the stagnation point of the impinging aerosol ($v = 0$) from Eqs. 7 and 8, considering steady state and one dimension

$$j_{tot} = \sum_{dm=0}^{\infty} \left(\frac{D_{dm}}{\delta_F} N_a(d_m) \right) + \frac{v_T}{\delta_T} N_p \quad (10)$$

where N_p is the total primary particle concentration computed previously at 20 cm HAB, δ_F and δ_T are the fluid and thermal boundary layer thickness, respectively, here approximated by δ. Therefore, the diffusion and thermophoretic fluxes are

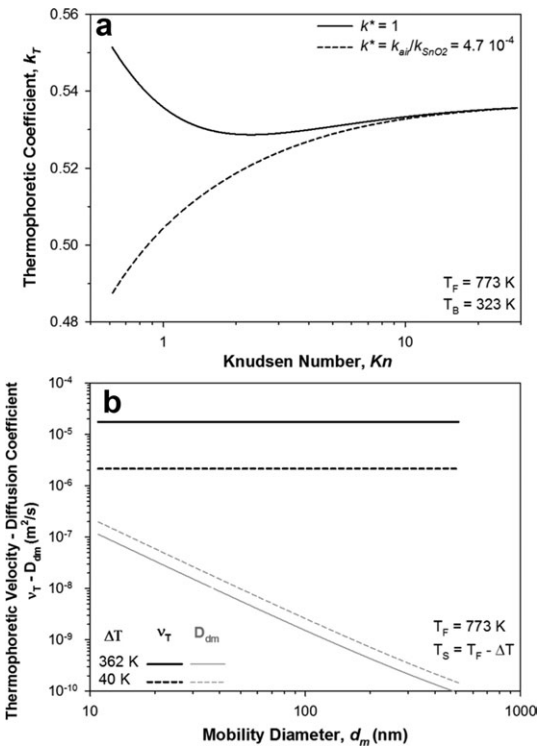

Figure 6. Thermophoretic coefficient (a) as a function of *Kn* computed either accounting for the fractal-like morphology of the particles ($k^* = 1$, continuous line) or from the thermal conductivity ratio of SnO_2 and air ($k^* = 4.7 \times 10^{-4}$, broken line).

Thermophoretic velocity ($k_T = 0.55$) and diffusion coefficient (b) as a function of the particle mobility diameter.

directly proportional to D_{dm} and v_T, respectively.

Figure 6b shows the thermophoretic velocity (black lines) and the diffusion coefficient (gray lines) as a function of the mobility diameter for high (continuous lines) and small (broken lines) temperature differences (ΔT) between the aerosol (T_F) and the substrate surface (T_S). The thermophoretic velocity (Figure 6b, black lines) decreased from 1.7×10^{-5} to 2.1×10^{-6} m^2/s with the temperature difference (ΔT) decreasing from 362 to 40 K. In contrast, the diffusion coefficient (Figure 6b, gray lines) doubled with ΔT decreasing from 362 to 40 K, due to the increasing T_p, but was always more than an order of magnitude smaller than v_T. With respect to the measured mobility geometric mean diameter (109 nm), the thermophoretic velocity and, thus, particle flux is expected to be about 2–3 order of magnitude (Figure 6b) higher than that generated by Brownian diffusion. As a result, even for surface temperatures (T_S) fairly close (e.g., $\Delta T = 40$ K) to the aerosol one (T_F), the contribution of diffusion seems negligible. This may apply also to considerably lower particle concentrations (Table 2) as even for 1/10th of the precursor feed rate used here, a geometric mean mobility diameter of 50 nm was measured[8] at 20 cm HAB for FSP-made TiO_2 nanoparticles. This mobility diameter would still lead (Figure 6b) to a diffusion coefficient about two orders of magnitude smaller than the expected thermophoretic velocity. As a result, the contribution of Brownian motion ($D_{dm} \ll v_T$) was neglected, and the particle flux to the substrate was computed from Eq. 10 and Eq. 8 independently of the mobility size

$$j_{tot} = 0.55 \frac{\mu_F}{\rho_F} \frac{(T_F - T_S)}{\delta_T \cdot T_P} N_p \tag{11}$$

where T_p is the particle temperature, here, approximated by the average of the aerosol (T_F) and surface (T_S) temperatures.

Following Eq. 11, a precise estimation of the surface temperature (T_S) is required to compute correctly the thermophoretic flux as T_S can be considerably above the temperature measured inside the substrate holder (T_B). This is particularly difficult when T_S approaches the aerosol temperature (T_F), as any uncertainty in T_S measurement will result in a larger relative error in the computation of the thermophoretic velocity. For example, an error of ± 20 K in the measurement of T_S results in an error of 7–12% and 30–100% in v_T at $\Delta T = 362$ and 40 K, respectively. To minimize this error, here, T_S was first measured (Figure 7a) for the lowest substrate holder temperature ($T_B = 323$ K) and, thus, highest ΔT. The T_S at higher T_B were, thereafter, estimated by the heat-transfer coefficient (h_T, W/m^2 K) computed at $T_B = 323$ K by the following correlation[55]

$$h_T = \frac{T_S - T_B}{T_F - T_S} \rho_T \tag{12}$$

where ρ_T is the thermal resistance of the substrate and its holder from the surface to the position of the thermocouple (Figure 1).

Figure 7a shows the measured T_S by a thermocouple (gray line) and an IR detector (circles) as a function of the aerosol deposition time (t_d) for a substrate holder (T_B) temperature of 323 K at 20 cm HAB ($T_F = 773$ K). Upon exposure to the aerosol, T_S (Figure 7a, circles) increased rapidly (60 s) from 312 to 410 K leading to a homogenous temperature

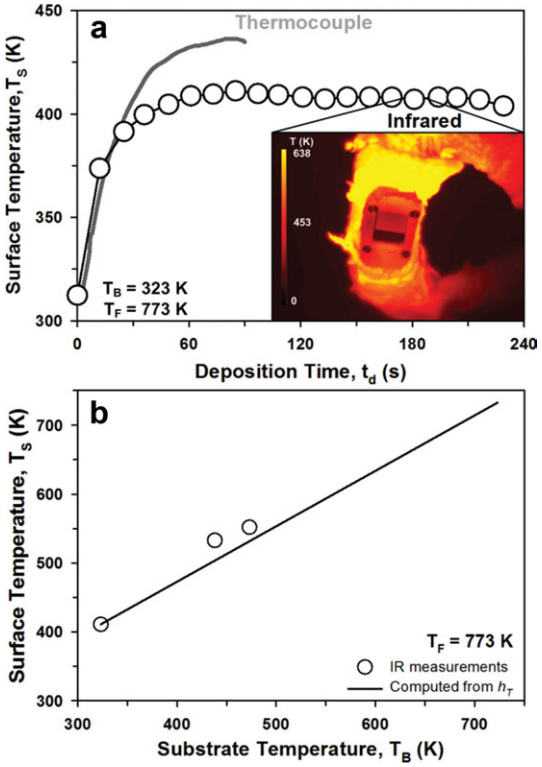

Figure 7. Measurement (a) of the surface temperature (T_S) of an alumina substrate during aerosol deposition by IR (circles) and with a thermocouple (line).

After starting the liquid-fed flame (a), at a constant T_B of 323 K, the T_S increased rapidly from nearly 323 to about 420 K within 60 s. (b) Expected (line) and measured (circles) surface temperature as a function of the substrate holder temperature (T_B). [Color figure can be viewed in the online issue, which is available at wiley onlinelibrary.com.]

profile on the substrate surface (Figure 7a, inset). The T_S measured by thermocouple (Figure 7a, lines) was about 20 K higher than that measured by IR (Figure 7a, circles). This is attributed to the nonideal contact between the thermocouple and the substrate surface leading to slightly higher temperatures. This steady-state T_S measured by IR (Figure 7a, circles) was used in Eq. 12 leading to a heat-transfer coefficient (h_T) of 602 W/m^2 K. Figure 7b shows the predicted (line) and IR-measured (circles) steady-state surface temperature (T_S) as a function of T_B. The estimated T_S (Figure 7b, line), following Eq. 12, was reasonably close to that measured by IR. This confirms that in this range of parameters the heat-transfer coefficient (h_T) is independent of the substrate temperature and can be used to estimate T_S in line with previous reports.[55] Here, these estimates of T_S (Figure 7b, line) were further used to compute the thermophoretic nanoparticle flux to the substrate according to Eq. 11.

Figure 8 shows the film mass (m_d) measured on the substrate (triangles) as a function of the aerosol (SnO_2, $C_{pr} = 0.5$ mol/L) deposition time (t_d) at 20 cm HAB ($T_F = 773$ K) and a substrate holder temperature (T_B) of 323 K ($T_S = 410$ K). The film mass (m_d) increased linearly with t_d indicating a constant nanoparticle deposition rate at least up to a visible film thickness of 71 μm (0.96 mg/cm^2). Constant film growth rates were also reported (Table 2) for aerosol

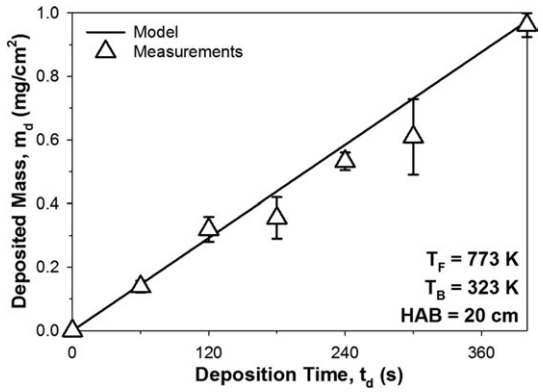

Figure 8. Deposited (triangles) and expected (lines) film mass as function of the deposition time (t_d) for an aerosol temperature (T_F) of 773 K and a substrate temperature (T_B) of 323 K at 20 cm HAB.

The film mass increased linearly with t_d indicating a constant deposition rate.

deposition of flame-made TiO_2[8,53] and Eu:Y_2O_3[14] nanoparticles. More in details, such FSP-made Eu:Y_2O_3 films having a porosity of 97% had a constant growth rate at least up to a visible film thickness of 239 μm[14] suggesting that film growth does not influence the nanoparticle deposition mechanism/rate. This is in agreement with the rapid achievement of a steady-state surface temperature (Figure 7a) indicating a constant thermophoretic flux. In fact, the film growth rate was reasonably well predicted (Figure 8, line) by the thermophoretic flux computed according to Eq. 11 with a boundary layer thickness (δ) of 0.4 mm. A constant nanoparticle deposition rate was also measured up to a substrate holder temperature (T_B) of 623 K corresponding to a ΔT of 121 K. Increasing further T_B to 723 K led to large variation in the measured deposition rate. This was attributed to the smaller temperature difference ($\Delta T = 40$ K) driving the thermophoretic flux at this high T_B (723 K) resulting in a larger amount of material being deposited during the unsteady state thermophoretic flux ($t_d \leq 60$ s) and, thus, yielding larger variance in the deposition rates.

Figure 9 shows the measured average nanoparticle deposition rate (triangles) during SnO_2 deposition ($C_{pr} = 0.5$ mol/L) at 20 cm HAB ($T_F = 773$ K) as a function of ΔT ($T_F - T_S$). Decreasing ΔT from 362 to 40 K decreased the nanoparticle deposition rate (Figure 9, triangles) from 0.14 to 0.06 mg/cm^2 min. This is in agreement with Eq. 11 predicting a rapid drop in the nanoparticle flux (Figure 9, line) with decreasing thermophoretic driving force ΔT. For the small ΔT ($\leq$121 K), the deposition rates computed here (Figure 9, line) underestimated considerably the measured ones (Figure 9, triangles). As discussed earlier, this is attributed to the initial warm up of the substrate surface (T_S) that result in a higher initial nanoparticle flux. These results (Figure 9) shows that up to a ΔT of 221 K, the nanoparticle deposition rate and, thus, film growth are reasonably well predicted by a steady-state thermophoretic model Eq. 11 that accounts for the substrate surface temperature (T_S) and dilution of the nanoparticle aerosol. At small temperature gradients ($\leq$121 K), a more detailed, time-dependent analysis seems necessary to describe the deposition dynamics sufficiently well. However, it should be considered that such small temperature gradients are unusual for flame deposition of nanoparticles (Table 2) as convective-driven self-cooling of the substrate usually leads to a considerable difference between aerosol (T_F) and substrate surface (T_S) temperatures.

Following these results for SnO_2, a more general estimation of the nanoparticle (molar) deposition flux for FSP systems was obtained for sufficiently large ΔT from Eqs. 1 and 11

$$j_{\text{tot-mol}} = 0.55 \frac{\mu_F \cdot d}{K_E \cdot \text{HAB} \cdot \delta} \frac{\Delta T}{T_P} \frac{\dot{V}_{pr}}{\dot{V}_{pr}\rho_{pr} + \dot{V}_{gas}\rho_{gas}} C_{pr} \quad (13)$$

where ρ_{pr} and ρ_{gas} are the initial precursor solution and gas flow densities, and ΔT and T_P can be calculated or measured directly as discussed earlier. For $\dot{V}_{gas} \ll \dot{V}_{pr}$, Eq. 13 predicts that the molar flow to the substrate ($j_{\text{tot-mol}}$) is nearly independent from the used precursor feed rate ($\dot{V}_{pr}$). However, as in this study, $\dot{V}_{gas}$ is usually[58] comparable or even greater than $\dot{V}_{pr}$ and, thus, variation of their ratio influences the deposition rate.

Figure 10 shows the molar deposition rate computed (line) by Eq. 13 for a temperature difference (ΔT) of 362 K at 20 cm HAB with the used flame settings (Table 1) as a function of the precursor concentration. The expected molar deposition rate (line) increased linearly from 10^{-7} to 10^{-6} mol/cm^2 min with increasing precursor concentration (C_{pr}) from 0.05 to 0.5 mol/L. This is attributed to a similar air entrainment and temperature difference (ΔT) for all concentrations resulting in a linear dependence of the deposition rate from the precursor solution concentration in Eq. 13. The predicted deposition rates (Figure 10, line) were reasonably well in agreement with those measured for FSP-synthesis (with the same nozzle geometry) and aerosol-deposition (Table 2) of TiO_2,[8] Eu:Y_2O_3,[14] and SnO_2 nanoparticles at about 20 cm HAB for different precursor feed rate and compositions. More in details, even if the precursor feed rate ($\dot{V}_{pr}$) was increased from 5 to 12 mL/min for deposition of SnO_2 (Figure 9, triangles) and Eu:Y_2O_3 (Figure 9, square) nanoparticles, respectively, they resulted in nearly the same deposition rate. This is attributed to the higher air entrainment for higher precursor feed rates that results in higher dilution of the nanoparticle aerosol. Furthermore, it should be noted that Eu:Y_2O_3 deposition was performed at 24 cm HAB and, thus, in slightly more diluted condition than for SnO_2 (20 cm HAB).

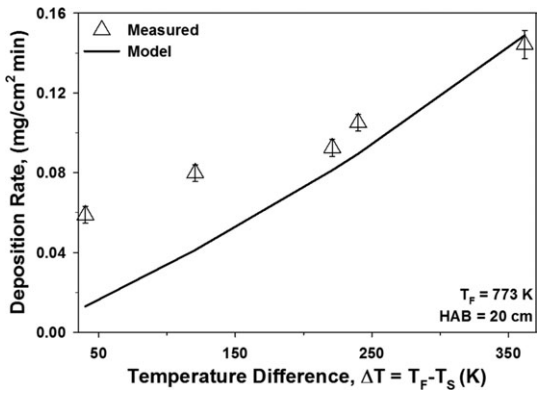

Figure 9. Modeled (line) and measured (triangles) average deposition rates as a function of the temperature difference (ΔT) between flame (T_F) and substrate surface (T_S).

With decreasing ΔT, the deposition rate prediction becomes less precise due to the increasing contribution of the unsteady state part of the particle flux.

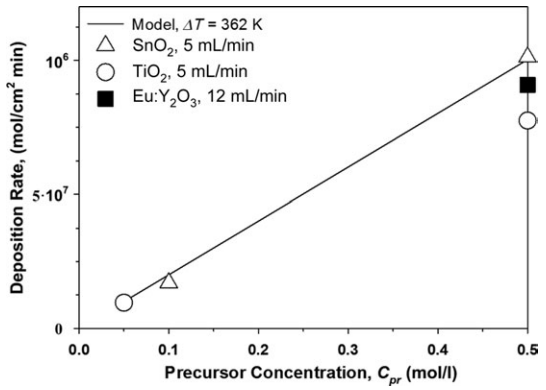

Figure 10. Expected molar deposition rate (line) as a function of the precursor concentration (C_{pr}) for a ΔT = 362 K at 20 cm HAB with the flame setting used in Table 1.

The developed thermophoretic model predicts reasonably well the deposition rates (Table 2) of TiO_2 (circles) at C_{pr} = 0.5 (this work) and 0.05 mol/L,[8] Eu:Y_2O_3 (square),[14] and SnO_2 (triangles, this work) nanoparticles for different precursor feed rates and concentrations.

The difference in deposition rate observed for SnO_2, Eu:Y_2O_3, and TiO_2 (circles) at a precursor concentration of 0.5 mol/L (Figure 9) are also attributed to the different substrates used that may have led to difference in the surface temperature (T_S) and to the different solvents (e.g., xylene, EtOH, and EHA) that results in different aerosol temperatures (T_F).

Conclusions

The deposition of nanoparticles (SnO_2 and TiO_2) from flame-spray pyrolysis reactors to temperature-controlled substrates was investigated as a function of the temperature difference (ΔT) between the aerosol and the substrate surface. For SnO_2, the deposited nanoparticle mass increased linearly with the deposition time indicating a constant deposition rate. The latter was mainly controlled by ΔT suggesting that thermophoresis was the main deposition mechanism at least up to a ΔT of 121 K. The predominance of thermophoresis was attributed to the rapid formation of agglomerates with large mobility diameters (>100 nm) having increased drag and, thus, considerably low diffusion coefficients. As a result, the nanoparticle deposition rate was reasonably well predicted by a constant thermophoretic flux computed from the aerosol and substrate surface temperatures. Nevertheless, at low temperature difference ($\Delta T \leq 121$ K), the deposition rate estimated by a constant thermophoretic flux underestimated considerably the measured ones. This was attributed to the initial phase of the deposition, where the actual substrate surface temperature was lower than the steady state one leading to momentary but significantly higher thermophoretic flux. This effect was more pronounced at low ΔT as small variations in the surface temperature have higher influence on the resulting thermophoretic flux.

The primary particle concentration of an exemplary (C_{pr} = 0.5 mol/L), flame-generated SnO_2 aerosol was estimated (2.94×10^{17} #/m^3 at STP) at 20 cm HAB by the enthalpy and precursor feed rates, and the measured aerosol temperature. This concentration was found in good agreement with that computed from the measured mobility number size distribution accounting for the fractal-like structure of the agglomerates and the primary particle size (10 nm). More in specific, the flame-made SnO_2 nanoparticles had already formed large agglomerates just above the flame tip (HAB = 13 cm) and, at 20 cm HAB, they reached a mobility mode and a geometric mean diameter of 131 and 137 nm, respectively. The comparison between the estimated primary particle concentration and the mobility count size distribution indicated that these SnO_2 agglomerates had a fractal dimension of about 2. At 20 cm HAB, the entrainment of surrounding air was estimated to 353 L/min at STP resulting in a dilution factor of 54.3 and an air entrainment constant of 0.23.

These results suggested that the nanoparticles molar deposition rate for similar flame-made aerosols (e.g., TiO_2) can be computed directly from the initial precursor concentration and enthalpy feed rate once the air entrainment constant is estimated. This assumption was validated against previously reported deposition rates for FSP-made TiO_2 and Eu:Y_2O_3 nanoparticles showing to be fairly robust against change in the precursor solution composition and deposition height. The presented model allows the computation of the nanoparticle deposition rate from flame-spray pyrolysis reactors without detailed knowledge of the air entrainment dynamics and aerosol properties. As a result, this approach could be rapidly implemented for a wide range of nozzle design and flame settings.

Acknowledgments

The authors are grateful to Dr. F. Krumeich (EMEZ, ETHZ) for the SEM and TEM analysis, Dr. H. Keskinen for the help with the SMPS analysis, Mr. K. Goossens for the help with the gravimetric measurement and to Prof. S.E. Pratsinis for fruitful discussion on the characterization of the aerosol properties and particle deposition dynamics. Financial support was provided by ETH Zurich.

Literature Cited

1. Borgarello E, Kiwi J, Pelizzetti E, Visca M, Gratzel M. Photochemical cleavage of water by photocatalysis. *Nature*. 1981;289:158–160.
2. Wu NL, Wang SY, Rusakova IA. Inhibition of crystallite growth in the sol–gel synthesis of nanocrystalline metal oxides. *Science*. 1999;285:1375–1377.
3. Oregan B, Gratzel M. A Low-cost, high-efficiency solar-cell based on dye-sensitized colloidal TiO_2 films. *Nature*. 1991;353: 737–740.
4. Lee SH, Kim YH, Deshpande R, Parilla PA, Whitney E, Gillaspie DT, Jones KM, Mahan AH, Zhang SB, Dillon AC. Reversible lithium-ion insertion in molybdenum oxide nanoparticles. *Adv Mater*. 2008;20: 3627–3632.
5. Kim H, Kim J, Yang H, Suh J, Kim T, Han B, Kim S, Kim DS, Pikhitsa PV, Choi M. Parallel patterning of nanoparticles via electrodynamic focusing of charged aerosols. *Nat Nanotechnol*. 2006;1: 117–121.
6. Mädler L, Roessler A, Pratsinis SE, Sahm T, Gurlo A, Barsan N, Weimar U. Direct formation of highly porous gas-sensing films by in-situ thermophoretic deposition of flame-made Pt/SnO_2 nanoparticles. *Sens Actuators B: Chem*. 2006;114:283–295.
7. Tricoli A, Graf M, Mayer F, Kühne S, Hierlemann A, Pratsinis SE. Micropatterning layers by flame aerosol deposition-annealing. *Adv Mater*. 2008;20:3005–3010.
8. Tricoli A, Righettoni M, Pratsinis SE. Anti-fogging nanofibrous SiO_2 and nanostructured SiO_2–TiO_2 films made by rapid flame deposition and in situ annealing. *Langmuir*. 2009;25:12578–12584.
9. Joshi RK, Kruis FE, Dmitrieva O. Gas sensing behavior of $SnO_{1.8}$:Ag films composed of size-selected nanoparticles. *J Nanoparticle Res*. 2006;8:797–808.
10. Tricoli A, Righettoni M, Teleki A. Semiconductor gas sensors: dry synthesis and application. *Angew Chem Int Ed*. 2010;49:7632–7659.
11. Tricoli A, Pratsinis SE. Dispersed nanoelectrode devices. *Nat Nanotechnol*. 2010;5:54–60.
12. Liu Y, Zha SW, Liu ML. Novel nanostructured electrodes for solid oxide fuel cells fabricated by combustion chemical vapor deposition (CVD). *Adv Mater*. 2004;16:256–260.
13. Thimsen E, Rastgar N, Biswas P. Rapid synthesis of nanostructured metal-oxide films for solar energy applications by a flame aerosol reactor (FLAR). *Solar Hydrogen Nanotechnol II*. 2007; 6650:G6500-G.

14. Kubrin R, Tricoli A, Camenzind A, Pratsinis SE, Bauhofer W. Flame aerosol deposition of Y_2O_3:Eu nanophosphor screens and their photoluminescent performance. *Nanotechnology*. 2010;21: 225603–225609.
15. Chew SY, Patey TJ, Waser O, Ng SH, Büchel R, Tricoli A, Krumeich F, Wang J, Liu HK, Pratsinis SE, Novák P. Thin nanostructured $LiMn_2O_4$ films by flame spray deposition and in situ annealing method. *J Power Sources*. 2009;189:449–453.
16. Thybo S, Jensen S, Johansen J, Johannessen T, Hansen O, Quaade UJ. Flame spray deposition of porous catalysts on surfaces and in microsystems. *J Catal*. 2004;223:271–277.
17. Rodriguez-Perez D, Castillo JL, Antoranz JC. Relationship between particle deposit characteristics and the mechanism of particle arrival. *Phys Rev E*. 2005;72:021403–021411.
18. Rodriguez-Perez D, Castillo JL, Antoranz JC. Density scaling laws for the structure of granular deposits. *Phys Rev E*. 2007;76:011407–011411.
19. Elmøe TD, Tricoli A, Grunwaldt J-D, Pratsinis SE. Filtration of nanoparticles: evolution of cake structure and pressure-drop. *J Aerosol Sci*. 2009;40:965–981.
20. Mädler L, Lall AA, Friedlander SK. One-step aerosol synthesis of nanoparticle agglomerate films: simulation of film porosity and thickness. *Nanotechnology*. 2006;17:4783–4795.
21. Keskinen H, Tricoli A, Marjamäki M, Mäkelä JM, Pratsinis SE. Size-selected agglomerates of SnO_2 nanoparticles as gas sensors. *J Appl Phys*. 2009;106:084316–084323.
22. Rosner DE, Khalil YF. Particle morphology- and Knudsen transition-effects on thermophoretically dominated total mass deposition rates from "coagulation-aged" aerosol population. *J Aerosol Sci*. 2000;31: 273–292.
23. Heine MC, Madler L, Jossen R, Pratsinis SE. Direct measurement of entrainment during nanoparticle synthesis in spray flames. *Combust Flame*. 2006;144:809–820.
24. Garcia-Ybarra PL, Castillo JL. Mass transfer dominated by thermal diffusion in laminar boundary layers. *J Fluid Mech*. 1997;336: 379–409.
25. Pratsinis SE. Flame aerosol synthesis of ceramic powders. *Prog Energy Combust Sci*. 1998;24:197–219.
26. Karthikeyan J, Berndt CC, Tikkanen J, Wang JY, King AH, Herman H. Preparation of nanophase materials by thermal spray processing of liquid precursors. *Nanostruct Mater*. 1997;9:137–140.
27. Tikkanen J, Gross KA, Berndt CC, Pitkanen V, Keskinen J, Raghu S, Rajala M, Karthikeyan J. Characteristics of the liquid flame spray process. *Surf Coat Technol*. 1997;90:210–216.
28. Athanassiou EK, Grass RN, Stark WJ. Chemical aerosol engineering as a novel tool for material science: from oxides to salt and metal nanoparticles. *Aerosol Sci Technol*. 2010;44:161–172.
29. Mädler L, Kammler HK, Mueller R, Pratsinis SE. Controlled synthesis of nanostructured particles by flame spray pyrolysis. *J Aerosol Sci*. 2002;33:369–389.
30. Friedlander SK, Fernandez de la Mora J, Gokoglu SA. Diffusive leakage of small particles across the dust-free layer near a hot wall. *J Colloid Interface Sci*. 1988;125:351–355.
31. Messerer A, Niessner R, Poschl U. Thermophoretic deposition of soot aerosol particles under experimental conditions relevant for modem diesel engine exhaust gas systems. *J Aerosol Sci*. 2003;34: 1009–1021.
32. Arabi-Katbi OI, Pratsinis SE, Morrison PW, Megaridis CM. Monitoring the flame synthesis of TiO_2 particles by in-situ FTIR spectroscopy and thermophoretic sampling. *Combust Flame*. 2001; 124:560–572.
33. Sahm T, Mädler L, Gurlo A, Barsan N, Pratsinis SE, Weimar U. Flame spray synthesis of tin dioxide nanoparticles for gas sensing. *Sens Actuators B: Chem*. 2004;98:148–153.
34. Tricoli A, Graf M, Pratsinis SE. Optimal doping for enhanced SnO_2 sensitivity and thermal stability. *Adv Funct Mater*. 2008;18:1969–1976.
35. Mädler L, Pratsinis SE. Bismuth oxide nanoparticles by flame spray pyrolysis. *J Am Ceram Soc*. 2002;85:1713–1718.
36. Tricoli A, Righettoni M, Pratsinis SE. Minimal cross-sensitivity to humidity during ethanol detection by SnO_2–TiO_2 solid solutions. *Nanotechnology*. 2009;20:315502–315511.
37. Zhu WH, Pratsinis SE. Synthesis of SiO_2 and SnO_2 particles in diffusion flame reactors. *AIChE J*. 1997;43:2657–2664.
38. Landgrebe JD, Pratsinis SE. Gas-phase manufacture of particulates—interplay of chemical-reaction and aerosol coagulation in the free-molecular regime. *Ind Eng Chem Res*. 1989;28:1474–1481.
39. Vemury S, Pratsinis SE. Self-preserving size distributions of agglomerates. *J Aerosol Sci*. 1995;26:175–185.
40. Heine MC, Pratsinis SE. Brownian coagulation at high concentration. *Langmuir*. 2007;23:9882–9890.
41. Kim DS, Hong SB, Kim YJ, Lee KW. Deposition and coagulation of polydisperse nanoparticles by Brownian motion and turbulence. *J Aerosol Sci*. 2006;37:1781–1787.
42. Han DH, Mungal MG. Direct measurement of entrainment in reacting/nonreacting turbulent jets. *Combust Flame*. 2001;124:370–386.
43. Skandan G, Glumac N, Chen YJ, Cosandey F, Heims E, Kears BH. Low-pressure flame deposition of nanostructured oxide films. *J Am Ceram Soc*. 1998;81:2753–2756.
44. Liu Y, Koep E, Liu ML. Highly sensitive and fast-responding SnO_2 sensor fabricated by combustion chemical vapor deposition. *Chem Mater*. 2005;17:3997–4000.
45. Karageorgakis NI, Heel A, Graule T, Gauckler LJ. Flame spray deposition of nanocrystalline dense $Ce_{0.8}Gd_{0.2}O_2$ - δ thin films: deposition mechanism and microstructural characterization. *Solid State Ionics*. 2011;192:464–471.
46. Vukasinovic B, Sundell S, Oljaca M. Closed loop controlled deposition of $Ba_xSr_{1-x}TiO_3$ thin films in spray flames. *Surf Eng*. 2003;19: 179–184.
47. Krinke TJ, Fissan H, Deppert K. Deposition of aerosol nanoparticles on flat substrate surfaces. *Phase Transitions*. 2003;76:333–345.
48. Kennedy MK, Kruis FE, Fissan H, Mehta BR, Stappert S, Dumpich G. Tailored nanoparticle films from monosized tin oxide nanocrystals: particle synthesis, film formation, and size-dependent gas-sensing properties. *J Appl Phys*. 2003;93:551–560.
49. Rogak SN, Flagan RC, Nguyen HV. The mobility and structure of aerosol agglomerates. *Aerosol Sci Technol*. 1993;18:25–47.
50. Lall AA, Friedlander SK. On-line measurement of ultrafine aggregate surface area and volume distributions by electrical mobility analysis. 1. Theoretical analysis. *J Aerosol Sci*. 2006;37:260–271.
51. Sorensen CM. The mobility of fractal aggregates: a review. *Aerosol Sci Technol*. 2011;45:765–779.
52. Kammler HK, Beaucage G, Mueller R, Pratsinis SE. Structure of flame-made silica nanoparticles by ultra-small-angle X-ray scattering. *Langmuir*. 2004;20:1915–1921.
53. Thimsen E, Biswas P. Nanostructured photoactive films synthesized by a flame aerosol reactor. *AIChE J*. 2007;53:1727–1735.
54. Hinds WC. *Aerosol Technology: Properties, Behavior and Measurement of Airbone Particles*. New York: Wiley, 1982.
55. Viskanta R. Heat-transfer to impinging isothermal gas and flame jets. *Exp Thermal Fluid Sci*. 1993;6:111–134.
56. Talbot L, Cheng RK, Schefer RW, Willis DR. Thermophoresis of particles in a heated boundary-layer. *J Fluid Mech*. 1980;101:737–758.
57. Batchelor GK, Shen C. Thermophoretic deposition of particles in gas flowing over cold surfaces. *J Colloid Interface Sci*. 1985;107:21–37.
58. Strobel R, Pratsinis SE. Flame aerosol synthesis of smart nanostructured materials. *J Mater Chem*. 2007;17:4743–4756.

Manuscript received Sept. 30, 2011, revision received Nov. 18, 2011, and final revision received Jan. 10, 2012.